30th Congress of the International Council of the Aeronautical Sciences
DCC, Daejeon, Korea ; September 25-30, 2016

FLUID-STRUCTURE INTERACTION ANALYSIS REGARDING THE INFLUENCE OF STRUCTURAL BOUNDARY CONDITION ON A FLAPPING WING

Haeseong Cho*, Namhun Lee, SangJoon Shin*, Seungsoo Lee**, and SangYong Kim*****
***Seoul National University, Republic of Korea, **Inha University, Republic of Korea**
****** Agency for Defense Development, Republic of Korea**

Keywords: *Fluid-Structure Interaction, Flapping wing, Co-rotational (CR) shell*

Abstract

In this paper, a fluid-structure interaction analysis is developed for a flapping wing. In order for the structural analysis, a co-rotational shell element is developed. It is for consideration with regard to the realistic three-dimensional wing configuration. Moreover, three-dimensional preconditioned Navier-Stokes equations are employed for the fluid analysis. Using the present FSI analysis, an explicit investigation for three-dimensional plunging wing with NACA0012 cross-section is conducted.

1 Introduction

Flapping wing micro air vehicles are envisioned as having a small maximum dimension, smaller than 15 cm, flying at low-Reynolds-number aerodynamic environment. Most of these vehicles are biologically inspired. Usefulness of the flapping wing vehicles has been expected during the long history of the natural flyer studies. The study of an interaction between the flexible structure and aerodynamics, fluid-structure interaction (FSI), is an important factor for design of the flapping wing MAV's. Many researchers' efforts upon the FSI characteristics of the flapping wing vehicles provide the physical understanding of the flow field around the wings [1-2].

One related study for the structural flexibility on the wing performance is the experiment conducted by Heathcote, et al [3]. In Heathcote's experiment, three kinds of the wing having NACA0012 cross-section (rigid, flexible, and highly flexible wings) were experimented. The parametric study with respect to the wing flexibility was carried out. The influence on the wing aerodynamic performance was then examined. As a result, a moderate amount of the flexibility can improve the wing aerodynamic performance, otherwise, significant degradation in the performance can be induced. This research becomes a representative benchmarking problem for validating the FSI analysis. A number of the previous computational studies have employed Heathcote's experiment in their validation procedure.

Chimakurthi et al. and Gordnier et al. [4-6] built a numerical framework to facilitate the FSI simulation on the flexible flapping wings at variable fidelity levels. A finite volume based Navier-Stokes fluid dynamics solver and a finite-element structural dynamic solver based on the geometrically nonlinear composite beam were included in their framework. Moreover, the structural analysis was extended by employing a co-rotational (CR) shell element. They were capable of good agreements between the numerical results and the results of Heathcote's experiment in a few cases. However, there also exist uncorrelated results in the case of the highly flexible wing.

In this paper, those uncorrelated results regarding the structural analysis, i.e., the wing boundary condition, will be further investigated. Hence, an improved FSI analysis will be constructed by using the nonlinear co-rotational

(CR) shell element. It is in order for consideration of the realistic three-dimensional wing configuration, and improvement on the accuracy of the structural analysis. Such structural analysis will be coupled with preconditioned Navier-Stokes solutions. Using the present FSI analysis, an explicit investigation regarding the three-dimensional wing with NACA0012 cross-section is conducted. In this procedure, the influence of the structural boundary condition on the coupled results will be carefully demonstrated and compared with the results from the previous studies [4-6].

2 Formulation

2.1 Co-rotational shell analysis

In this paper, the nonlinear shell element based on the CR formulation is developed. The CR formulation is one such approach which is applicable for geometrically nonlinear problems in the structural analysis.

Based on the assumptions of a small degree of strain and large displacement, the CR formulation allows an accurate geometrically nonlinear structural analysis. The main advantage of the CR formulation is that it leads to artificial separation between the material and the geometrical nonlinearity. Therefore, a local formulation is required for the small deformational component, and this is done by using the existing finite element hypothesis. This concept was originally developed by Rankin et al. during the derivation procedure of what is known as the element-independent co-rotational (EICR) description [7]. Felippa and Haugen [8] suggested a unified formulation of the CR formulation and discussed its usefulness as related to the EICR concept.

Figure 1 shows the coordinates used in the formulation. During the derivation of the CR formulation, the geometrical nonlinearity from the material response of the element is induced by decoupling the rigid body components. Due to the assumption that the pure deformation is small in the local CR frame, the geometrically linear finite element formulation can be used in the local system between the CR frame and the deformed frame.

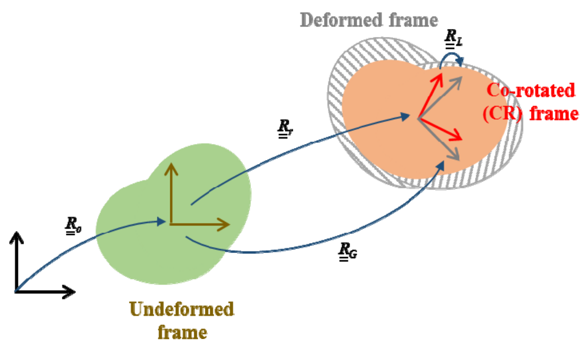

Fig. 1. Coordinate system of the CR formulation

Consistent transformation of element stiffness matrix and internal force vector from the local system to the global coordinate system is accomplished. As a result the geometrically nonlinear effects are included. Details of its mathematics, presented in Ref. [9, 10], can be summarized as follows:

$$d_g = E^T d_l \tag{1}$$

$$\begin{gathered} f_g = E^T f_l \\ K_g = E^T K_l E + \partial\left(E^T f_l\right) / \partial d_g \end{gathered} \tag{2}$$

where d, f, and K is the displacement, internal force vectors, and stiffness matrix, respectively. E and $\partial\left(E^T\right) / \partial d_g$ represent the transformation matrices. Those matrices are constructed with regard to the element frame in order to re-express displacement, internal force vectors, and stiffness matrix.

By maintaining the above manner as well as the consideration of the nodal DOF's, it is possible to compose various nonlinear finite elements. This suggests that the procedure in Eqs. (1)-(2) will be applicable to the CR shell element by only expanding the transformation matrices to 18 DOF's (for the 3-node shell element). In the present analysis, a facet shell element combining an optimal triangular membrane with discrete Kirchhoff triangular bending plate (OPT-DKT) is used for the local element [11].

The final form the nonlinear dynamic equation can be obtained as follows.

$$F_{dyn}(\ddot{x},\dot{x},x,t)+F_g(x,t)=F_{ext}(t) \tag{3}$$

In order to solve the nonlinear dynamic equation, Hilber-Hughes-Taylor (HHT)–α method is employed [12].

2.2 Aerodynamic model

2.1.1 Governing equations

To analyze flows around the flapping wings at low Mach and Reynolds number regime, three-dimensional preconditioned Navier-Stokes equations are chosen as the governing equations. A differential form of the non-dimensional governing equations with free stream conditions is written as:

$$\Gamma\frac{\partial Q_p}{\partial \tau}+\frac{\partial W}{\partial t}+\nabla\cdot\vec{F}=\nabla\cdot\vec{F}_v, \tag{4}$$

where W is the conservative solution vector, Q_p is the primitive solution vector, $\vec{F}$ is the inviscid flux vector, and $\vec{F}_v$ is the viscous flux vector.

For accurate unsteady computations, a fictitious time derivative term is added as can be seen in Eq. (4). A preconditioning matrix, Γ of Weiss and Smith [13] is adopted for accurate and efficient computations for low Mach number flows.

2.1.2. Numerical schemes

The numerical algorithm used in this paper is based on a finite volume method (FVM). For the discretization of the inviscid flux vector, Roe’s approximated Riemann solver [14] is used. MUSCL extrapolation with van Albada’s limiter is adopted to obtain the higher spatial accuracy while maintaining the total variation diminishing (TVD) property. The derivatives of the solution vectors are computed at the cell interfaces by applying the gradient theorem over an auxiliary cell. These derivatives are used to compute the viscous flux vector, which is equivalent to the second order central difference method on a regular grid. For unsteady flow analysis, a dual time stepping method in conjunction with approximate factorization-alternate direction implicit (AF-ADI) method is used to discretize the fictitious time derivative term of the governing equations.

2.1.2 Deformation of the grids

A radial basis function (RBF) interpolation is employed for a deforming grid technique. Good quality grids can be created from the deformed wing surface grids by the RBF interpolation method [15, 16]. For efficient construction of the interpolation function, a greedy algorithm suggested in [17] is used. The conjugate gradient method is used to solve the linear equations.

2.1.3 Geometric conservation law

For evaluation of the volume of computational cells with the deforming grids, only geometric consideration is not enough to ensure that the uniform flow is a solution to the Navier-Stokes equations [18]. The Geometric Conservation Law (GCL) is adopted to alleviate the problem.

2.3 Coupling methodology

To couple the aerodynamic model with the structural model, an implicit coupling method is adopted. In the implicit coupling method, FSI coupled solutions are obtained in an iteratively manner by exchanging the results more than once every sub-iteration. A linear interpolation scheme is employed for the exchange between the different boundary of the fluid and the structural domain. Thus, the aerodynamic load vectors are interpolated into the nodal force vector. Subsequently, the nodal displacement vector is interpolated into the surface grid information for the CFD solver. Detailed description of the coupling algorithm is explained in Ref. [19]. Figure 2 shows a diagram of the present coupling algorithm.

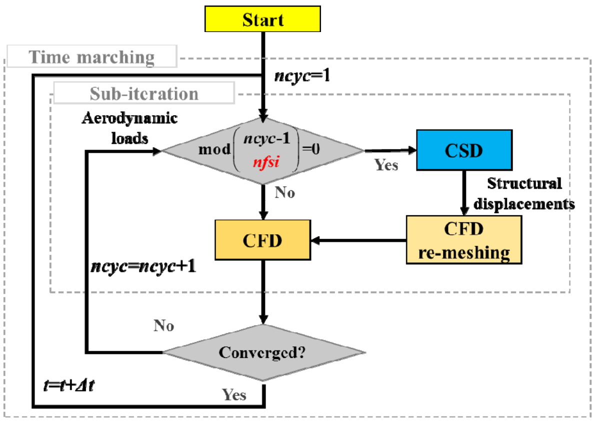

Fig. 2. Diagram of the present coupling algorithm [19]

3 Numerical results

In this section, verification of the present FSI analysis is conducted. Moreover, the influence of the structural boundary condition on the coupled results is investigated and compared with experimental results by Heathcote et al. [3] and numerical results from the previous studies [4-6]. In this paper, the flexible and highly flexible wings are considered. The relevant analysis condition is summarized in Table 1, and the structural properties of three rectangular wings (NACA0012 cross section) are presented in Table 2.

Table. 1. Experimental conditions

Classification	Value	Classification	Value
Reynolds number	30000	**Plunge amplitude**	0.0175m
Flow velocity (U_∞)	0.3m/s	**Prescribed motion**	Cosine
Water density	1000 kg/m^3	**Reduced frequency, k_G ($2\pi f/U_\infty$)**	0~1.82

Table. 2. Properties of the wings

Classification	Flexible	Highly Flexible
Semi-span width	0.3m	0.3m
Chord length	0.1m	0.1m
Thickness	0.001m	0.001m
Poisson's ratio	0.3	0.3
Material density	7,800 kg/m^3	2,700 kg/m^3
Young's modulus	210 GPa	40 GPa

3.1 Structural modeling approach for NACA0012 plunging wing

Figure 3 shows the experiment performed by Heathcote et al. [3]. The configuration of the wing is indicated by the dotted line. As shown in the figure, the wing is neither cantilevered nor slender. The forepart of the wing root is connected to the region A. Moreover, the relevant boundary condition should be clearly assigned by observing the experimental condition. Thus, a shell analysis can be an appropriate approach for such experimental situation, when compared to a beam analysis.

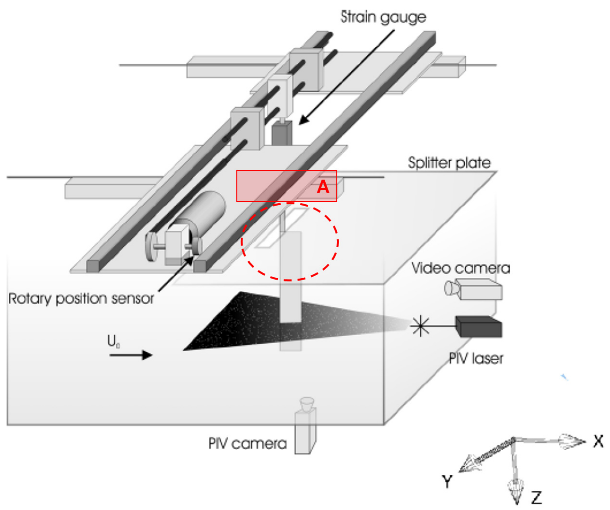

Fig. 3. Experiment of the rectangular wings [3]

Hence, structural analyses under both cantilevered boundary condition and leading-edge-fixed boundary condition are conducted. The relevant structural boundary conditions are illustrated in Fig. 4. The wing is discretized by using 936 triangular shell elements, accounting up to 3,120 degrees of freedom.

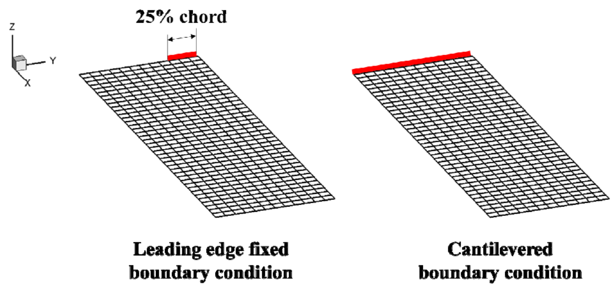

Fig. 4. Structural boundary condition of the flexible and highly flexible wings

3.2 FSI results at the reduced frequency = 1.82

In this section, the FSI results obtained by the present analysis will be presented, and comparison with the previous studies [4-6] will be conducted. Moreover, the influence on the FSI phenomena over the wing at the reduced frequency (k_G) 1.82 will be described with respect to the wing root boundary condition.

3.2.1 Comparison with the previous studies

In this subsection, the present predictions are compared with those obtained from the previous studies and the experiment. Figure 5 shows comparison of the thrust coefficient history, and Fig. 6 shows the thrust coefficient history of each wing. The averaged thrust coefficient is then compared. The relevant values are summarized in Tables 3 and 4. Differences are presented by subtraction of the physical values. All the present results are described by the abbreviations, i.e., L.E. and Cant. for the leading-edge-fixed and cantilevered boundary conditions, respectively.

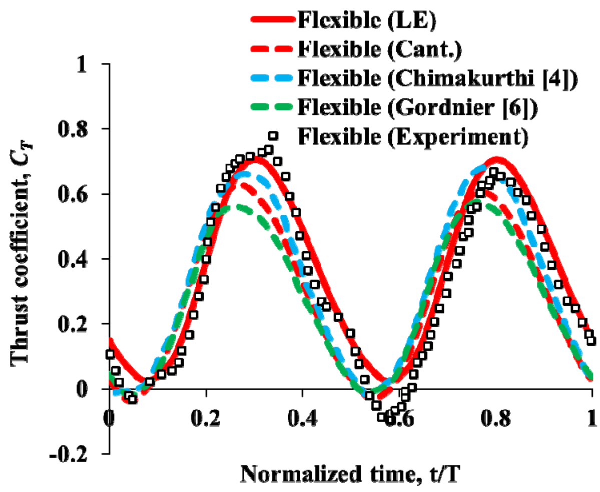

Fig. 5. Thrust coefficient history of the flexible wing

Table. 3. Comparison of the averaged C_T of the flexible wing

	Flexible	Difference
Present (L.E.)	0.35	0.03
Present (Cant.)	0.29	0.03
Chimakurthi et al. [4]	0.31	0.01
Gordnier et al. [6]	0.278	0.042
Experiment [3]	0.32	-

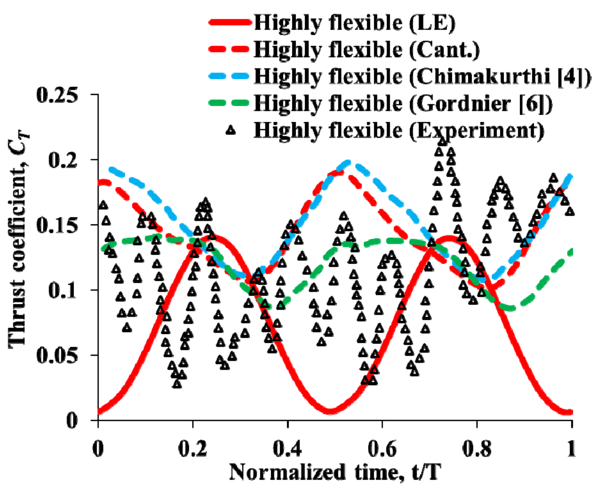

Fig. 6. Thrust coefficient history of the highly flexible wing

Table. 4. Comparison of the averaged C_T of the highly flexible wing

	Highly flexible	Difference
Present (L.E.)	0.07	0.04

Present (Cant.)	0.15	0.04
Chimakurthi et al. [4]	0.16	0.05
Gordnier et al. [6]	0.12	0.01
Experiment [3]	0.11	-

For the flexible wing, the present thrust coefficient history shows good agreement with that observed in the experiment. Also, the present prediction regarding the highly flexible wing shows similar trend with that predicted in the previous studies. However, the high frequency response observed in the experiment was not captured in either predictions. Extensive investigation for such FSI phenomenon in the highly flexible wing is still required.

The wing tip displacement history of the wing tip is illustrated in Fig. 7. The peak-to-peak relative differences regarding the experimental results of the tip displacement history are summarized in Tables 5 and 6.

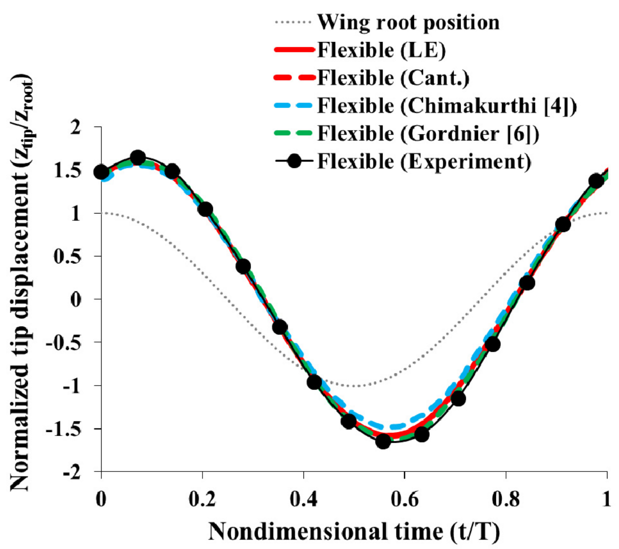

Fig. 7. Tip displacement history of the flexible wings

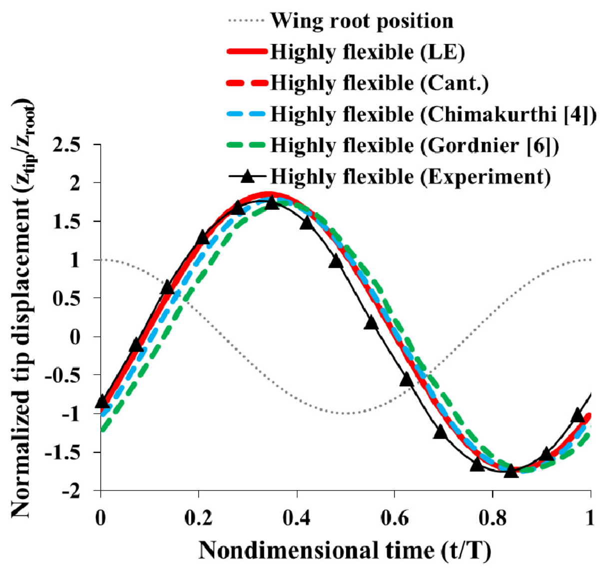

Fig. 8. Tip displacement history of the highly flexible wings

Table. 5. Comparison of the normalized peak-to-peak difference in the tip history of the flexible wing

	Flexible	Difference
Present (L.E.)	3.19	0.09
Present (Cant.)	3.17	0.11
Chimakurthi et al. [4]	3.12	0.16
Gordnier et al. [6]	3.20	0.08
Experiment [3]	3.28	-

Table. 6. Comparison of the normalized peak-to-peak difference in the tip history of the highly flexible wing

	Highly flexible	Difference
Present (L.E.)	3.62	0.10
Present (Cant.)	3.70	0.18
Chimakurthi et al. [4]	3.56	0.04
Gordnier et al. [6]	3.46	0.06
Experiment [3]	3.52	-

For the flexible wing, the present prediction shows good agreement with the experimental results. Regarding the structural flexibility, a phase variation in the tip history is induced due to the inertial and aerodynamic forces, and it becomes more significant for the highly flexible wing. Degrees of the phase variation is compared and summarized in Tables 7 and 8.

Table. 7. Comparison of the phase variation in the tip history of the flexible wing

	Flexible	Difference
Present (L.E)	25.5°	1.7°
Present (Cant.)	25.0°	2.2°
Chimakurthi et al. [4]	23.5°	3.7°
Gordnier et al. [6]	25.1°	1.9°
Experiment [3]	27.2°	-

Table. 8. Comparison of the phase variation in the tip history of the flexible wing

	Highly flexible	Difference
Present (L.E)	125°	8°
Present (Cant.)	123°	6°
Chimakurthi et al. [4]	126°	9°
Gordnier et al. [6]	135°	18°
Experiment [3]	117°	-

Regarding the structural boundary condition, there was no feasible improvement in the numerical prediction. However, for the highly flexible wing, significant decrease in the C_T history is predicted.

In the following section, the relevant comparison of the pressure coefficient on the wing surface with respect to the structural boundary conditions will be presented.

3.2.2 Influence of the wing root boundary condition

In this section, the pressure coefficient, C_P, on the wing surface is presented in order to evaluate the detailed influence of the wing structural boundary condition. The relevant situation for the comparison is illustrated in Fig. 9. Moreover, the relevant comparison between the present results of the flexible and highly flexible wings under the cantilevered and leading-edge fixed boundary conditions are presented in Figs. 10 and 11, respectively.

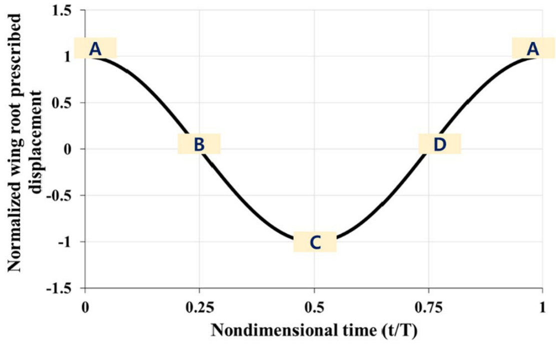

Fig. 9. Prescribed wing root displacement history

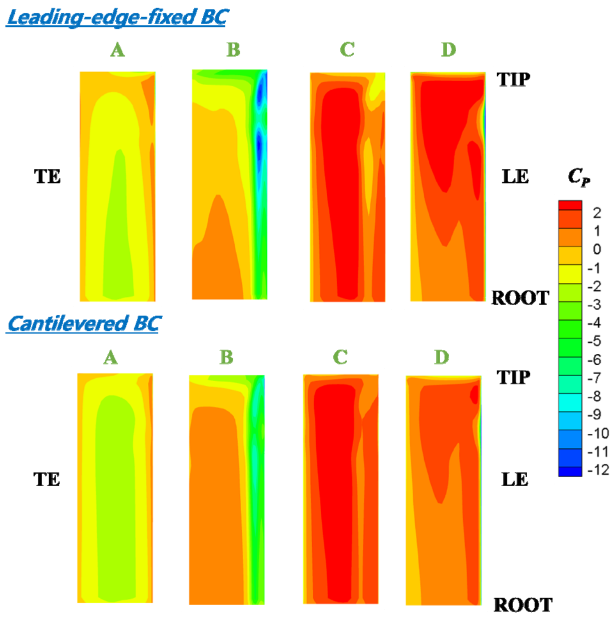

Fig. 10. Pressure distribution of the flexible wing

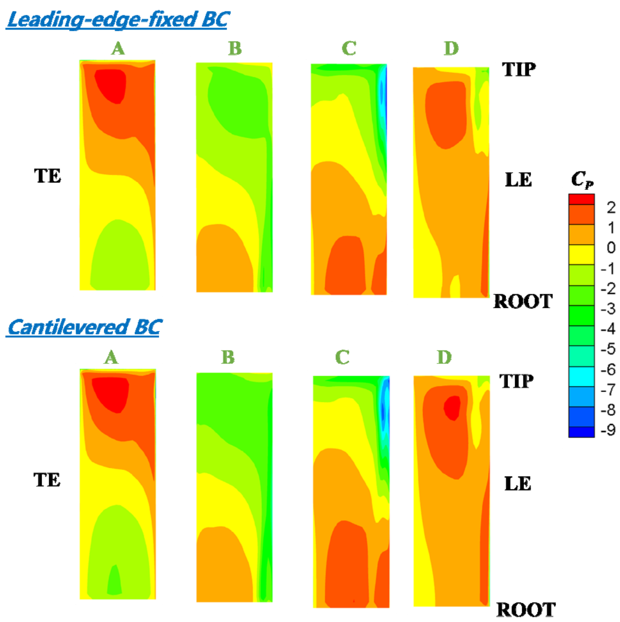

Fig. 11. Pressure distribution of the highly flexible wing

Pressure distribution of the flexible wing under the leading-edge-fixed boundary condition shows increased amount of C_P than that for the cantilevered wing. For the highly flexible wing, the distribution of C_P is slightly different. C_P variation of the wing under leading-edge-fixed boundary condition is weaker than that of the cantilevered wing is. Also, the present prediction shows the phase shift in the pressure distribution of the highly flexible wing. Such differences over the flexible and highly flexible wings are caused by the chordwise deformation of the wing. However, the presently adopted root boundary condition is not the major factor of the high frequency response in the highly flexible wing.

4 Conclusion

In this paper, an improved FSI analysis is constructed by using the nonlinear CR shell element. Such structural analysis is coupled with preconditioned Navier-Stokes solutions. Using the present FSI analysis, an explicit investigation regarding the three-dimensional wing with NACA0012 cross-section is conducted. In this procedure, the influence of the structural boundary condition on the coupled results is carefully evaluated and compared with the results from the previous studies. In both analyses using the present wing boundary conditions shows reasonable agreement with those from the experiment and the previous studies. Moreover, due to the chordwise flexibility of the wing under the leading-edge boundary condition, there exist a difference with the pressure coefficient on the wing surface. This phenomenon is clearly the case for the highly flexible wing, and it induces significant decrease in the thrust. However, there still exist factors which should be considered, i.e., assumption regarding Young's modulus of the highly flexible wing's aluminum plate to be 40GPa (its correct value is 70GPa) and the additional component connected to the wing root. In the future, those parameters will be included and investigated.

Acknowledgement

This work was supported by Advanced Research Center Program (NRF-2013R1A5A1073861) through the National Research Foundation of Korea(NRF) grant funded by the Korea government(MSIP) contracted through Advanced Space Propulsion Research Center at Seoul National University and also by a grant to Bio-Mimetic Robot Research Center Funded by Defense Acquisition Program Administration, and by Agency for Defense Development (UD130070ID).

References

[1] Shyy, W., Lian, Y., Tang, J., Viieru, D. and Liu, H., *Aerodynamics of Low Reynolds Number Flyers*, Cambridge University Press, New York, 2007.

[2] Smith, M. J. C., "The Effects of Flexibility on the Aerodynamics of Moth Wings: Towards the Development of Flapping-Wing Technology," *33rd Aerospace Sciences Meeting and Exhibit*, Reno, Nevada, 1995.

[3] Heathcote, S., Wang, Z. and Gursul, I., "Effect of Spanwise Flexibility on Flapping Wing Propulsion," *Journal of Fluids and Structures*, Vol. 24, No. 2, 2008, pp. 183-199.

[4] Chimakurthi, S. K., Stanford, B. K., Cesnik, C. E. S. and Shyy, W., "Flapping Wing CFD/CSD Aeroelastic Formulation Based on a Corotational Shell Finite Element," AIAA-2009-2412, *50th AIAA / ASME / ASCE / AHS / ASC Structures, Structural Dynamics, and Materials Conference*, Palm Springs, CA, May 4-7, 2009.

[5] Chimakurthi, S. K., Tang, J., Palacios, R., Cesnik, C. E. S. and Shyy, W., "Computational Aeroelasticity Framework for Analyzing Flapping Wing Micro Air Vehicles," *AIAA Journal*, Vol. 47, No. 8, 2009, pp. 1865-1878.

[6] Gordnier, R.E., Chimakurthi, S.K., Cesnik, C.E.S., Attar, P.J., "High-fidelity aeroelastic computations of a flapping wing with spanwise flexibility," *Journal of Fluids and Structures*, Vol. 40, pp. 86-104, 2013.

[7] Rankin, C. C. and Nour-Omid, B., "An Element-independent Corotational Procedure for the Treatment of Large Rotations," *ASME Journal of Pressure Vessel Technology*, Vo. 108, No. 2, 1989, pp. 165-175.

[8] Felippa, C. and Haugen, B., "A Unified Formulation of Small Strain Corotational Finite Elements: I. Theory," *Computational Methods in Applied Mechanics and Engineering*, Vol. 194, pp. 2285-2335, 2005.

[9] Pacoste, C., "Corotational Flat Facet Triangular Elements for Shell Instability Analysis," *Computer Methods in Applied Mechanics and Engineering*, Vol. 156, No. 1-4, 1998, pp. 75-110.

[10] Battini, J. -M., and Pacoste, C., "On the Choice of Local Element Frame for Corotational Triangular Shell Elements," *Computer Methods in Applied Mechanics and Engineering*, Vol. 20, No. 10, 2004, pp. 819-825.

[11] Khosravi, R., Ganesan, R. and Sedaghati, R., "An Efficient Facet Shell Element for Co-rotational Nonlinear Analysis of Thin and Moderately Thick Laminated Composite Structures," *Computers and Structures*, Vol. 86, pp. 850-858, 2008.

[12] Crisfield, M. A., *Non-Linear Finite Element Analysis of Solids and Structures, Advanced Topics, Vol. 2*. Wiley, Chis Chester, 1997.

[13] Weiss, J.M., and Smith, W.A., "Preconditioning applied to variable and constant density flows," *AIAA Journal*, Vol. 33, No. 11, 1995, pp. 2050-2057.

[14] Roe, P.L., "Approximate Riemann Solvers, Parameter Vectors, and Difference Schemes," *Journal of Computational Physics*, Vol. 32, 1981, pp. 357-372.

[15] Rendall, T.C.S., and Allen, C.B., "Unified fluid-structure interpolation and mesh motion using radial basis functions," *Int. J. Numer. Meth. Engng*, Vol. 74, Issue. 10, 2008, pp. 1519-1559.

[16] Wright, G.B., "Radial basis function interpolation: numerical and analytical developments," Ph.D. Dissertation, University of Colorado, Denver, USA, 2003.

[17] Schaback, R., and Wendland, H., "Adaptive greedy techniques for approximate solution of large RBF systems," *Numerical Algorithms*, Vol. 24, Issue. 3, 2000, pp. 239-254.

[18] Thomas, P.D., and Lombard, C.K., "The Geometric Conservation Law A-Link Between Finite-Difference and Finite-Volume Methods of Flow Computation on Moving Grids," AIAA Paper 78-1208, 1978.

[19] Cho, H., Kwak, J. Y., Shin, S. J., Lee, N. and Lee, S., "Flapping Wing Fluid-Structural Interaction Analysis using Co-rotational Triangular Planar Structural Element," *AIAA Journal*, accepted for publication, 2016.

Copyright Statement